

Stabilized imaging of immune surveillance in the mouse lung

Mark R Looney^{1,4}, Emily E Thornton^{2,4}, Debasish Sen², Wayne J Lamm³, Robb W Glenny³ & Matthew F Krummel²

Real-time imaging of cellular and subcellular dynamics in vascularized organs requires image resolution and image registration to be simultaneously optimized without perturbing normal physiology. This problem is particularly pronounced in the lung, in which cells may transit at speeds $>1 \text{ mm s}^{-1}$ and in which normal respiration results in large-scale tissue movements that prevent image registration. Here we report video-rate, two-photon imaging of a physiologically intact preparation of the mouse lung that is stabilizing and noninvasive. Using our method, we obtained evidence for differential trapping of T cells and neutrophils in mouse pulmonary capillaries, and observed neutrophil mobilization and dynamic vascular leak in response to stretch and inflammatory models of lung injury in mice. The system permits physiological measurement of motility rates of $>1 \text{ mm s}^{-1}$, observation of detailed cellular morphology and could be applied in the future to other organs and tissues while maintaining intact physiology.

The lung is a unique organ with an air-liquid interface exposing it to the environment and to a large volume of blood that transits the organ each minute. The lung microcirculation is also distinctive with a rich network of capillary segments with diameters as small as a few micrometers, which requires many leukocytes to deform their shape to pass through¹. In fact, as compared to systemic vascular beds, the initial sequestration of neutrophils in the lung microcirculation is more dependent on mechanical forces than adhesion-mediated rolling along the endothelial surfaces². Any perturbation to the integrity of the lung's air-liquid interface can have devastating consequences, resulting in lung vascular leak and compromised gas exchange. Furthermore, the nature of the collaboration between immune cells and structural elements of the lung has been inaccessible for real-time analysis.

The uniqueness of the lung requires direct imaging, but this demands fast, high-resolution and penetrant imaging methodologies as well as demonstrable maintenance of intact physiology. The lung provides a particular challenge as it propagates motion resulting from cardiac contractions, pulsatile blood flow and overall movements during the inhalation-exhalation cycle³.

Compared to the sub-micrometer resolution demanded by analysis of deformability, these movements are on the scale of millimeters when measured at the pleural face of the lung. Previous protocols for imaging in the lung have relied on methods such as isolation and reperfusion of the lung *ex vivo*⁴, clamping of ventilation⁵ or capturing images at the end of lung expiration (end-expiration) or after cessation of mechanical ventilation⁶. Although each of these approaches has been useful for lung imaging, an improvement was needed to study high-speed, three-dimensional cellular dynamics under physiological gas exchange and blood flow.

We addressed these issues via an optimized, resonant-scanning, two-photon platform⁷. In our method we adopted point-scanning multiphoton imaging, which provides excellent depth penetration. The depth (z dimension) resolution across many air-liquid alveolar interfaces severely influences the coherence of light at the focus. Multiphoton excitation, with its inherent requirement for high-photon densities, is resistant to image degradation, compared to single-photon approaches. Resonant scanning permits acquisition at or exceeding video rate⁸, thus providing high temporal resolution over large cross-sectional areas. Finally, and most importantly, we optimized a gentle stabilization system, which limits tissue motion, even while permitting intact blood flow at predicted rates and providing continuous access to inhaled gases. We used this system to describe immune cell circulation and cellular movement under steady-state physiology and in lung inflammation and injury models. Our results suggest surveillance of the alveolar-capillary interface from the bloodstream.

RESULTS

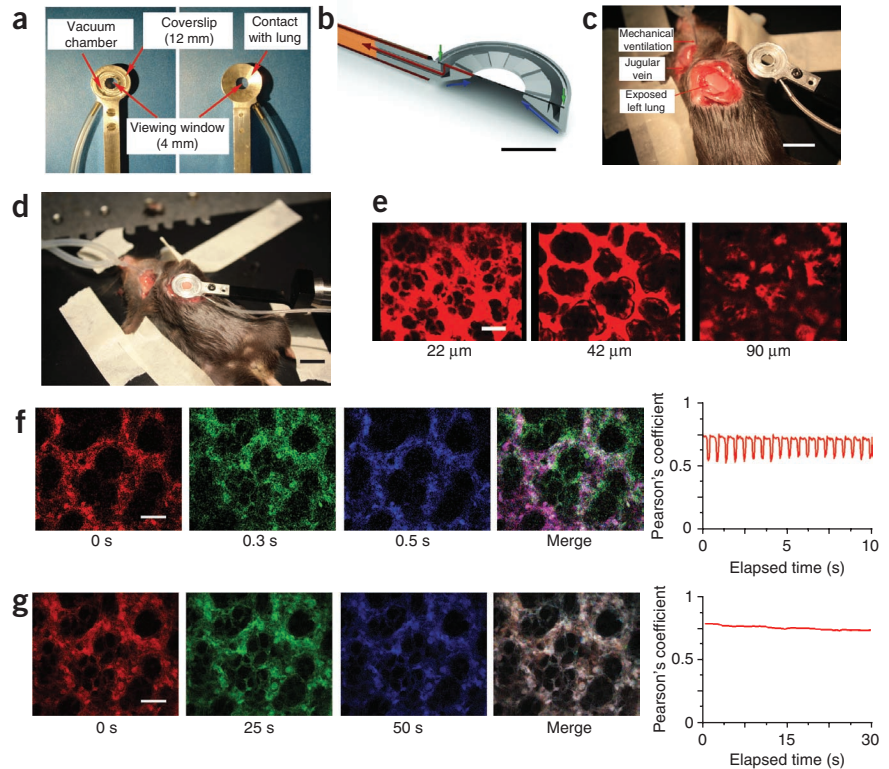
Experimental setup and stabilization

To stabilize the lung for imaging in a live animal with minimal disruption of ventilation or circulation, we constructed a thoracic window^{3,9}, modified for the mouse with a 4-mm internal diameter (Fig. 1a,b). An important feature of this device is its loose adherence to the lung surface via 20–25 mm Hg of reversible vacuum spread over a large local area allowing for gas to enter and expand the lung but limiting the associated movement in the x , y and z dimensions. The vacuum in this device circulates through grooves adjacent to the imaging area and gently pulls the tissue

¹Departments of Medicine and Laboratory Medicine, University of California, San Francisco, San Francisco, California, USA. ²Department of Pathology, University of California, San Francisco, San Francisco, California, USA. ³Department of Medicine, University of Washington, Seattle, Washington, USA. ⁴These authors contributed equally to this work. Correspondence should be addressed to M.F.K. (matthew.krummel@ucsf.edu).

Figure 1 | Experimental setup and image stability for intravital imaging of the mouse lung.

(a) Anterior and posterior views of the thoracic suction window fitted with a coverslip. (b) Side-view rendering of the suction window showing suction chamber, cover slip (green arrows) and vacuum flows (blue arrows near tissue, red arrows toward suction regulator). (c) Surgical preparation of left thorax with exposed left lung. (d) Suction window *in situ*. (e) Representative images at the indicated depths in a mouse injected with Texas Red-dextran, showing the capillary bed above (left) and below (right) the subpleural alveoli (middle). (f,g) Still images of CFP fluorescence in an actin-CFP-expressing mouse lung at the indicated times after the start of imaging (color-coded arbitrarily), and a merge of these three images (far right). The plot shows the Pearson's coefficient between time points. Images shown in f were captured at 30 fps. In g, each frame represents 15 integrated images that are then merged (time points aligned and the Pearson's coefficient from this integration is shown). Scale bars, 5 mm (b), 10 mm (c,d) and 50 μm (e-g).



into a shallow conical region facing an imaging-grade coverslip. The vacuum also effectively sets the coverslip in a small groove along the outside dimension of the device.

For the surgical preparation, we anesthetized the mice and performed a tracheotomy to facilitate mechanical ventilation. Then we placed mice in the right, lateral decubitus position and resected three left anterior ribs revealing the left, anterior lung surface (Fig. 1c). We positioned the thoracic suction window, attached to a rigid strut and a micromanipulator, immediately above the left lung and applied 20–25 mm Hg of suction to gently immobilize the lung throughout the respiratory cycle (Fig. 1d). We chose the least amount of suction that allowed the lung to enter the thoracic window and remain stabilized for visualization throughout the respiratory cycle. Although the applied suction is an increase above the negative pleural pressures in the intact thorax of spontaneously breathing mice¹⁰, we expected this pressure to dissipate in areas further away from the window itself, thus providing limited effects well within the range of two-photon excitation. Then we lowered the objective onto the 12-mm glass coverslip for imaging with our two-photon microscope (Supplementary Fig. 1a) in the central region of this preparation to minimize any effects of suction transmitted to the edges. We tested for any damage to the lungs from mechanical ventilation or thoracic suction using the gravimetric method to measure lung edema formation. We found no increase in lung edema after 2 h of continuous ventilation and thoracic suction (Supplementary Fig. 1b).

To determine whether there was still motion associated with inhalation-exhalation, we imaged alveolar inflation and deflation under suction window conditions (Supplementary Movie 1); this confirmed that ventilation was maintained in the portion of lung in the thoracic window. One of the important advantages of two-photon microscopy is tissue penetration beyond what is achievable with single-photon confocal approaches. We tested the tissue imaging depth range of our method by injecting Texas Red-dextran intravenously and scanning along the *z* axis. We captured

images at different depths down to 125 μm (Supplementary Fig. 1c), which allowed us to completely visualize the capillary bed above and under the subpleural alveoli (Fig. 1e).

We next tested the stability of images captured from our imaging system. Using mice that ubiquitously expressed CFP (actin-CFP), ventilated at 120 breaths per minute (bpm), we captured images at 30 frames per second (fps) of inspiration, expiration and inspiration again; overlay images from three subsequent time points revealed that the alveolar and microvascular structures were stable with our imaging technique (Fig. 1f and Supplementary Movie 2). Based on the limited movement of vessels even during respiration, we estimate that we reduced overall motion to ~5–10 μm in all dimensions.

To quantify the stability and the deflections induced by mechanical ventilation captured at 30 fps, we used the Pearson's coefficient to compare images between frames (Fig. 1f). This revealed that exactly four frames per breath are disrupted owing to ventilation (120 bpm), but that the image reliably returned to a stable baseline after each respiratory cycle, thus yielding 20 fps with exceptional 'colocalization' of tissue. Time-averaging (15 integrated video-rate frames) of our image acquisition also effectively averaged out the four out of sync frames owing to breathing (Fig. 1g and Supplementary Movie 3), producing low-noise images. An alternative approach to improve image stability was to remove the four frames in which breathing was occurring in postprocessing (Supplementary Fig. 1d). We also injected intravenous Texas Red dextran (molecular weight 70,000 Da) into wild-type mice to visualize the lung microcirculation. Our system stably captured these blood vessels and slow-moving cellular shadows within them (Supplementary Movie 4).

Perfusion and cellular behavior with thoracic suction

We next examined blood flow velocities in the lung contained in the thoracic window by intravenously injecting fluorescent

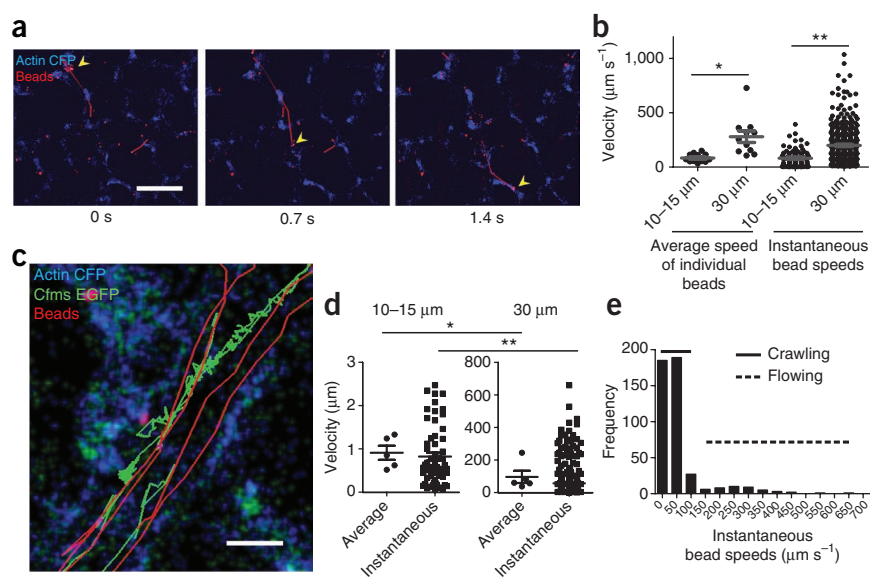


Figure 2 | Perfusion velocities of beads and neutrophils in the lung. **(a)** The micrographs show sequential images of individual beads traversing the lung microcirculation (arrowheads), in actin-CFP-expressing mice injected intravenously with red fluorescent microspheres and then imaged at 30 fps. Time elapsed after the first frame is indicated. Scale bar, 50 μm . **(b)** Perfusion velocities of individual beads shown as individual dots in small ($109 \pm 12 \mu\text{m s}^{-1}$, mean \pm s.e.m., $n = 14$) and medium-sized blood vessels ($280 \pm 53 \mu\text{m s}^{-1}$, mean \pm s.e.m., $n = 11$; $P < 0.001$). **(c)** The micrograph shows one frame recorded at 30 fps with four representative tracks of neutrophils (colony-stimulating factor 1R (Cfms)-EGFP) and beads inside a vessel of an actin-CFP-expressing mouse injected with fluorescent beads and imaged at 30 fps. Scale bar, 10 μm . **(d)** The plots show the average and instantaneous track speeds of neutrophils in small ($0.91 \pm 0.16 \mu\text{m s}^{-1}$, mean \pm s.e.m., $n = 5$) and medium-sized ($96.5 \pm 37.8 \mu\text{m s}^{-1}$, mean \pm s.e.m., $n = 5$, $*P < 0.05$ and $**P < 0.001$) blood vessels. **(e)** Histogram of neutrophil perfusion velocities in a medium-sized blood vessel. Solid line highlights cells that are crawling along the vessel at slow speeds, and dotted line highlights cells with velocities most consistent with flow within vessels.

microspheres (1- μm beads) into actin-CFP-expressing mice and tracking movement of the beads inside microvasculature using fast acquisition rates (30 fps). We tracked an individual red fluorescent microsphere during its transit through the imaging field of an 8–15 μm blood vessel (Fig. 2a). We quantified

diameter) and in larger vessels (30 μm average diameter) (Fig. 2c), and we calculated the individual transit velocities of these cells (Fig. 2d). We collected sequential images of neutrophils transiting a medium-sized blood vessel into which we also injected 1- μm red fluorescent beads (Fig. 2c and Supplementary Movie 6).

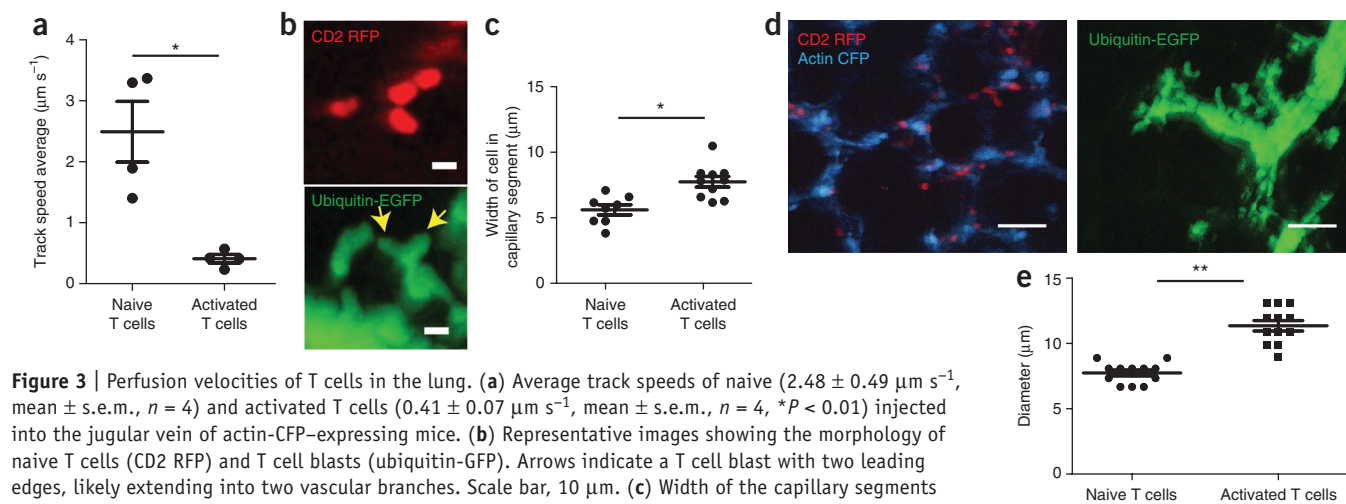


Figure 3 | Perfusion velocities of T cells in the lung. **(a)** Average track speeds of naive ($2.48 \pm 0.49 \mu\text{m s}^{-1}$, mean \pm s.e.m., $n = 4$) and activated T cells ($0.41 \pm 0.07 \mu\text{m s}^{-1}$, mean \pm s.e.m., $n = 4$, $*P < 0.01$) injected into the jugular vein of actin-CFP-expressing mice. **(b)** Representative images showing the morphology of naive T cells (CD2 RFP) and T cell blasts (ubiquitin-GFP). Arrows indicate a T cell blast with two leading edges, likely extending into two vascular branches. Scale bar, 10 μm . **(c)** Width of the capillary segments containing naive ($5.61 \pm 0.39 \mu\text{m}$, mean \pm s.e.m., $n = 8$) and activated T cells ($7.75 \pm 0.41 \mu\text{m}$, mean \pm s.e.m., $n = 12$, $*P < 0.01$) are plotted. **(d)** Maximal intensity projections of single time points showing the sizes of intravascular naive (left) and activated (right) T cells. Images are from 40 μm z-dimension stack. **(e)** Average diameters of naive ($7.74 \pm 0.23 \mu\text{m}$, mean \pm s.e.m., $n = 12$) and activated T cells ($11.36 \pm 0.40 \mu\text{m}$, mean \pm s.e.m., $n = 12$, $*P < 0.05$, $**P < 0.001$ and $P < 0.0001$).

the microsphere perfusion velocities by calculating instantaneous (frame to frame) and average (mean over entire observation period) track speeds (Online Methods); the majority of beads transited lung microvasculature at fast flow rates ($109 \pm 12 \mu\text{m s}^{-1}$, mean \pm s.e.m.; Fig. 2b) through this small-sized blood vessel (Fig. 2a and Supplementary Movie 5). We also calculated bead speeds through a larger vessel (30 μm in diameter), which yielded faster flow rates of $280 \pm 53 \mu\text{m s}^{-1}$ (Fig. 2b and Supplementary Movie 6). Our calculated perfusion velocities in these blood vessels are similar to those in previous reports in the lung and in systemic microvasculature not using stabilized window methods^{11,12}.

An important advantage of intravital imaging in the mouse is the availability of fluorescent reporter strains to facilitate cellular imaging, and we sought to couple our method with these to understand how specific cell types behave as they transit the lung. Most notably, it has not been possible to assess the extent to which neutrophils or T cells may ‘patrol’ the vasculature, given the extremely tight constrictions during their transit. We tracked the movement of endogenous LysM-EGFP⁺ (also known as LysM-GFP⁺) or Cfms-GFP⁺ neutrophils in both small capillary segments (10–15 μm average

EGFP⁺ neutrophils transited at $1.42 \pm 0.16 \mu\text{m s}^{-1}$ in capillary segments and at $97 \pm 38 \mu\text{m s}^{-1}$ in vessels that were roughly twice as large (Fig. 2d). In medium-sized vessels, we observed a bimodal distribution of neutrophil perfusion velocities, with one population of neutrophils transiting at speeds just below the rate of 1- μm beads and another population transiting much more slowly and rolling and even arresting along the endothelial surface (Fig. 2e and Supplementary Movie 6). Some individual neutrophils remained trapped for long periods and moved much more slowly even in larger-sized blood vessels, compared to the flow as calculated by the movement of much smaller beads. The heterogeneity of neutrophil transit velocities has been previously documented in the canine pulmonary circulation¹³. This suggests both trapping in narrow capillaries but also continuous scanning of the lung vasculature under rapid flow.

We next tested the contribution of cell size or activation state to intravascular cell velocities in the lung, and we observed a general trend in which larger and more activated cells move more slowly than naive ones: naive T cells (CD2-RFP) injected into the jugular vein moved with a velocity of $2.48 \pm 0.49 \mu\text{m s}^{-1}$ compared to T cells that had been activated for 4 d with their cognate antigen and with interleukin-2 (blasts), which transited at less than $0.5 \mu\text{m s}^{-1}$

(Fig. 3a). With the 0.6- μm resolution capacity of our two-photon microscope, we also detected that small (naive) T cells did not evidently adopt elongated ‘amoeboid’ characteristic morphology (Fig. 3b), even while they surveyed the capillary (Supplementary Movie 7). In contrast, larger, stimulated T cells were not only characteristically amoeboid but also made multiple projections, likely down two vessels at a junction (Fig. 3b). Furthermore, when we intravenously injected naive T cells into mice, we detected entry of T cells into the capillary segments of the lung, whereas T cell blasts were restricted to larger blood vessels and largely did not enter the capillary segments (Fig. 3c,d and Supplementary Movie 7). This differences in size of these two cell types likely explain the observed distribution (Fig. 3e).

Neutrophil dynamics in lung inflammation and injury

An important value in our system is that the lung continues to receive ventilation as it normally would and is under normal physiological blood flow, allowing for the direct examination of events when inhaled or intravascular agents first enter the lung. We used our imaging technique to examine, under different pathologic conditions, the cellular changes that occur as inhaled material enters the lung (Fig. 4). We imaged LysM-GFP mice injected

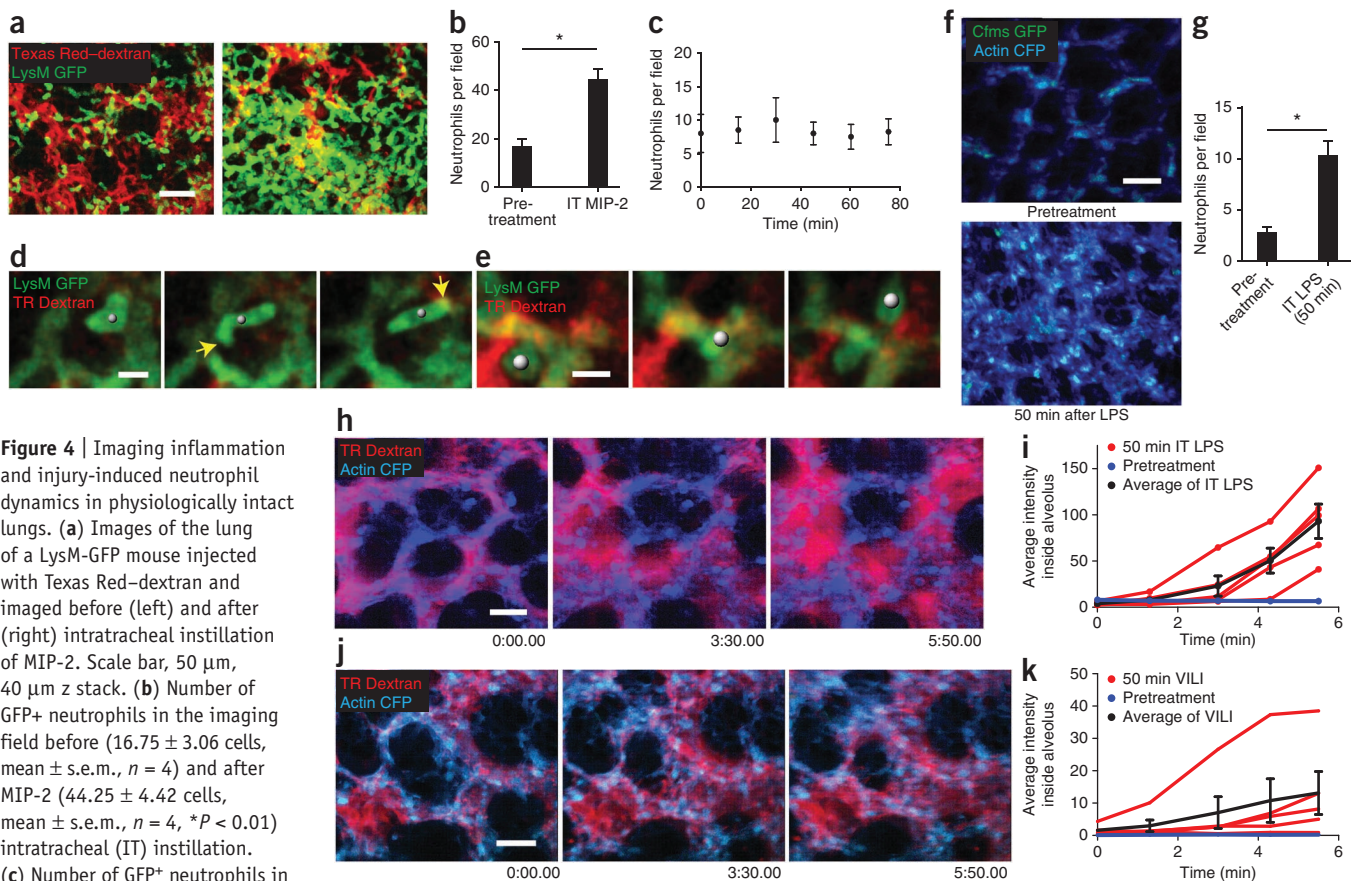


Figure 4 | Imaging inflammation and injury-induced neutrophil dynamics in physiologically intact lungs. (a) Images of the lung of a LysM-GFP mouse injected with Texas Red-dextran and imaged before (left) and after (right) intratracheal instillation of MIP-2. Scale bar, 50 μm , 40 μm z stack. (b) Number of GFP⁺ neutrophils in the imaging field before (16.75 ± 3.06 cells, mean \pm s.e.m., $n = 4$) and after MIP-2 (44.25 ± 4.42 cells, mean \pm s.e.m., $n = 4$, $*P < 0.01$) intratracheal (IT) instillation. (c) Number of GFP⁺ neutrophils in

the lung vasculature under continuous suction ($n = 4$ for each time point). (d) Representative images of an intravascular GFP⁺ neutrophil. Scale bar, 10 μm , single z plane at 5:20, 6:40 and 9:20 min:s. (e) Representative images of a GFP⁺ neutrophil moving within alveoli. Scale bar, 10 μm , single z plane at 0:40, 5:40 and 9:00 min:s. (f) Images of the lung of an actin-CFP/*c-fms*-GFP mouse before and after intratracheal instillation of LPS. Scale bar, 50 μm , 40 μm z stack. (g) Number of neutrophils per field before (2.75 ± 0.48 , mean \pm s.e.m., $n = 4$) and after LPS instillation (10.25 ± 1.32 , mean \pm s.e.m., $n = 4$, $*P < 0.01$). (h,j) Images of the lung of an actin-CFP mouse injected with Texas Red-dextran and either challenged with intratracheal LPS for 50 min (h) or subjected to ventilator-induced lung injury for 60 min (j). Scale bar, 50 μm , 40 μm z stack. (i,k) The plots show the average intensity of fluorescent dextran in the alveolar space at the indicated times after LPS treatment (i) or ventilator-induced lung injury (k). Blue lines are the pretreatment average ($n = 3$ alveoli), red lines are individual alveoli measured after treatment and black lines are the after treatment average ($n = 5$ alveoli).

with Texas Red–dextran before and after intratracheal challenge with the neutrophil chemokine, macrophage inflammatory protein-2 (MIP-2; 5 μg ; **Fig. 4a**). As we predicted based on still images from killed mice, we observed a large influx of GFP⁺ neutrophils after chemokine challenge (**Fig. 4b** and **Supplementary Movie 8**). In control experiments when LysM-GFP mice were continuously ventilated under suction window conditions for 75 min, there was no artificial recruitment of neutrophils over time (**Fig. 4c**). Intratracheal challenge with MIP-2 produced a dynamic scrum of cells; we observed neutrophil crawling in the intravascular compartment, with individual cells rapidly changing their leading and trailing edges (**Fig. 4d** and **Supplementary Movie 9**). Additionally, we identified mobile, extravascular neutrophils with rounded morphologies after chemokine challenge (**Fig. 4e** and **Supplementary Movie 10**). As this model provides global chemokine, it is perhaps not unexpected to see such active behaviors or intra-alveolar entry of cells. To examine a more physiological insult, we used a model of acute lipopolysaccharide (LPS) inflammation and injury, and identified similar neutrophil swarming after intratracheal LPS challenge (5 mg kg⁻¹; **Fig. 4f,g** and **Supplementary Movie 11**).

We also examined the dynamic leakage of dextran into the extravascular compartment, which is indicative of the increased lung vascular permeability characteristic of acute lung injury (**Fig. 4h** and **Supplementary Movie 12**). We quantified the average progressive increase in dextran leakage after intratracheal LPS; this revealed a differential rate of vascular leakage across the imaged alveoli (**Fig. 4i** and **Supplementary Movie 12**). This observation could not be made with common endpoint measurements (for example, bronchoalveolar-lavage protein measurements) of global lung vascular permeability.

Finally, we examined a model of ventilator-induced lung injury, an important contributor to excess mortality in critically ill individuals¹⁴. We visualized and quantified dextran leakage into the interstitial and alveolar spaces in mice challenged with lung stretch compared with normal tidal volumes (**Fig. 4j,k** and **Supplementary Movie 13**). Again, we observed heterogeneity in the rates of vascular leak among the imaged alveoli.

DISCUSSION

Our method does not involve interruption of ventilation with the attendant pulmonary vasoconstrictor response⁵ or artificial perfusion or removal of the organ from the host. Isolated, perfused lung preparations have been widely used in pulmonary research with great success and with the advantage of manipulating flow velocities and shear stresses^{15–17}. However, this technique does not retain lymphatic flow, circulation is interrupted so that recruitment of cells from the bone marrow or lymphatic system is not possible, and perfusion through an artificial circulation may have unintended consequences on cellular behavior.

Our technique preserves both ventilation and perfusion. The rates of blood flow were similar to values presumed from other organs, and there was visible evidence of ventilation, but this did not prevent imaging because the system reliably returns to the same location after a ventilatory cycle. Imaging throughout the respiratory cycle is an important technical advance over prior intravital lung preparations in which imaging either occurred with the interruption of ventilation or was timed for capture at only end expiration⁶. Finally, our approach is durable with no detectable injury to the stabilized

lung, and we routinely imaged for up to 3 h, which is the longest duration of imaging that we have attempted thus far.

Neutrophils uniquely traverse the lung compared to other tissues¹³, yet much of the studies of neutrophil rheology using intravital techniques have come from nonpulmonary organs, which may not accurately reflect the dynamics of the pulmonary microcirculation¹⁸. Neutrophil-mediated lung diseases, such as acute lung injury¹⁹, can now be studied directly. Our approach also permitted us to observe capture of multiple cell types and to measure dwell times for lymphocytes that reach the small capillary segments. This stalling effect may provide ample opportunity for both surveillance and also for lung-remodeling factors to be deposited; these details are now open to investigation using our approach. Our method should enable the study of both the onset of adaptive immune responses and the homing of metastatic tumors to the lung. Breast tumor metastases and normal breast ductal cells may establish residency in the lung²⁰; our method will enable the study of this process and possibly allow researchers to identify the supporting cells of the metastatic niche.

The limitations of our system include (i) imaging under positive pressure ventilation and not during spontaneous breathing, and (ii) imaging of only subpleural blood vessels and alveolar units, although we imaged up to 125 μm below the pleural surface, and the subpleural and deeper parenchymal microvascular networks are generally thought to be similar in terms of vascular regulation²¹. A recent study²² in which the authors used glue to fix the lung surface to a coverslip is a possible alternative method that may have similar benefits to those presented here, but the physiologic integrity of that preparation has yet to be established. Although our system substantially improves upon existing approaches, there is room for improvements. For example, adaptive optics has recently been used to overcome the distortions associated with changes in refractive index as two-photon light enters the target tissue²³. Such an approach would undoubtedly be beneficial in the lung, where light transverses many such interfaces at the surface of each subsequent air-filled alveolus. Advances in miniaturization, such as the use of gradient index lenses²⁴ or miniaturized lens elements, should also be possible, which may result in even less-invasive approaches that are possibly suitable for diagnostic thoracic imaging in humans.

METHODS

Methods and any associated references are available in the online version of the paper at <http://www.nature.com/naturemethods/>.

Note: Supplementary information is available on the Nature Methods website.

ACKNOWLEDGMENTS

We thank O. Khan for his side-view rendering of the thoracic suction window and N. Amodaj for software support. This work was supported in part by US National Institutes of Health grants K08 HL082742 (M.R.L.) and P01 HL024136 (M.F.K.), by the American Asthma Foundation and Sandler Basic Asthma Research Center (M.F.K.), by the National Blood Foundation (M.R.L.) and by the National Science Foundation Graduate Research Fellowships Program (E.E.T.).

AUTHOR CONTRIBUTIONS

M.R.L. conceived and designed the experiment, validated and implemented the technique, collected and analyzed data and wrote the manuscript. E.E.T. conceived and designed the experiment, validated and implemented the technique, collected and analyzed data and wrote the manuscript. D.S. implemented the technique and collected and analyzed data. W.J.L. conceived and designed the experiment and validated the technique. R.W.G. conceived and designed the experiment and edited the manuscript.

M.F.K. conceived and designed the experiment, provided administrative and financial support and wrote the manuscript.

COMPETING FINANCIAL INTERESTS

The authors declare no competing financial interests.

Published online at <http://www.nature.com/naturemethods/>.

Reprints and permissions information is available online at <http://npg.nature.com/reprintsandpermissions/>.

- Wiggs, B.R. *et al.* Contributions of capillary pathway size and neutrophil deformability to neutrophil transit through rabbit lungs. *J. Appl. Physiol.* **77**, 463–470 (1994).
- Burns, A.R., Smith, C.W. & Walker, D.C. Unique structural features that influence neutrophil emigration into the lung. *Physiol. Rev.* **83**, 309–336 (2003).
- Wagner, W.W. Jr. Pulmonary microcirculatory observations in vivo under physiological conditions. *J. Appl. Physiol.* **26**, 375–377 (1969).
- Kiefmann, R., Rifkind, J.M., Nagababu, E. & Bhattacharya, J. Red blood cells induce hypoxic lung inflammation. *Blood* **111**, 5205–5214 (2008).
- Hasegawa, A. *et al.* Color-coded real-time cellular imaging of lung T-lymphocyte accumulation and focus formation in a mouse asthma model. *J. Allergy Clin. Immunol.* **125**, 461–468 (2010).
- Tabuchi, A., Mertens, M., Kuppe, H., Pries, A.R. & Kuebler, W.M. Intravital microscopy of the murine pulmonary microcirculation. *J. Appl. Physiol.* **104**, 338–346 (2008).
- Bullen, A., Friedman, R.S. & Krummel, M.F. Two-photon imaging of the immune system: a custom technology platform for high-speed, multicolor tissue imaging of immune responses. *Curr. Top. Microbiol. Immunol.* **334**, 1–29 (2009).
- Nguyen, Q.T., Callamaras, N., Hsieh, C. & Parker, I. Construction of a two-photon microscope for video-rate Ca(2+) imaging. *Cell Calcium* **30**, 383–393 (2001).
- Lamm, W.J., Bernard, S.L., Wagner, W.W. Jr. & Glenny, R.W. Intravital microscopic observations of 15-microm microspheres lodging in the pulmonary microcirculation. *J. Appl. Physiol.* **98**, 2242–2248 (2005).
- Hoffman, A.M. *et al.* Matrix modulation of compensatory lung regrowth and progenitor cell proliferation in mice. *Am. J. Physiol. Lung Cell. Mol. Physiol.* **298**, L158–L168 (2010).
- Popel, A.S. & Johnson, P.C. Microcirculation and hemorrheology. *Annu. Rev. Fluid Mech.* **37**, 43–69 (2005).
- Waisman, D. *et al.* Subpleural microvascular flow velocities and shear rates in normal and septic mechanically ventilated rats. *Shock* **26**, 87–94 (2006).
- Gebb, S.A. *et al.* Sites of leukocyte sequestration in the pulmonary microcirculation. *J. Appl. Physiol.* **79**, 493–497 (1995).
- The Acute Respiratory Distress Syndrome Network. Ventilation with lower tidal volumes as compared with traditional tidal volumes for acute lung injury and the acute respiratory distress syndrome. *N. Engl. J. Med.* **342**, 1301–1308 (2000).
- Presson, R.G. Jr., Baumgartner, W.A. Jr., Peterson, A.J., Glenny, R.W. & Wagner, W.W. Jr. Pulmonary capillaries are recruited during pulsatile flow. *J. Appl. Physiol.* **92**, 1183–1190 (2002).
- Kuebler, W.M., Ying, X., Singh, B., Issekutz, A.C. & Bhattacharya, J. Pressure is proinflammatory in lung venular capillaries. *J. Clin. Invest.* **104**, 495–502 (1999).
- Bhattacharya, J. & Staub, N.C. Direct measurement of microvascular pressures in the isolated perfused dog lung. *Science* **210**, 327–328 (1980).
- Zarbock, A. & Ley, K. New insights into leukocyte recruitment by intravital microscopy. *Curr. Top. Microbiol. Immunol.* **334**, 129–152 (2009).
- Looney, M.R., Su, X., Van Ziffle, J.A., Lowell, C.A. & Matthay, M.A. Neutrophils and their Fc gamma receptors are essential in a mouse model of transfusion-related acute lung injury. *J. Clin. Invest.* **116**, 1615–1623 (2006).
- Podsypanina, K. *et al.* Seeding and propagation of untransformed mouse mammary cells in the lung. *Science* **321**, 1841–1844 (2008).
- Short, A.C. *et al.* Pulmonary capillary diameters and recruitment characteristics in subpleural and interior networks. *J. Appl. Physiol.* **80**, 1568–1573 (1996).
- Kreisel, D. *et al.* In vivo two-photon imaging reveals monocyte-dependent neutrophil extravasation during pulmonary inflammation. *Proc. Natl. Acad. Sci. USA* **107**, 18073–18078 (2010).
- Ji, N., Milkie, D.E. & Betzig, E. Adaptive optics via pupil segmentation for high-resolution imaging in biological tissues. *Nat. Methods* **7**, 141–147 (2010).
- Barretto, R.P., Messerschmidt, B. & Schnitzer, M.J. In vivo fluorescence imaging with high-resolution microlenses. *Nat. Methods* **6**, 511–512 (2009).

ONLINE METHODS

Mice. The following mice were used in our experiments: C57BL/6 wild-type (Charles River); *c-fms*-GFP²⁵ in which EGFP is driven under the CSF-1R promoter (highlights neutrophils, monocytes, and macrophages and were provided by Z. Werb (University of California San Francisco)); actin-CFP²⁶ have the CFP transgene ubiquitously expressed and were obtained from I. Weissman (Stanford University); CD2-RFP (expressing RFP in all T cells and a small subset of NK cells), OT-II TCR transgenic (OVA-specific Class II restricted), and ubiquitin-EGFP (EGFP expression in all cells) were obtained from The Jackson Laboratories. LysM-EGFP mice (EGFP expression in monocytes, macrophages and neutrophils) were obtained from E. Robey (University of California, Berkeley) (ref. 27). All experiments involving mice were approved by the Institutional Animal Care and Use Committee at the University of California, San Francisco.

Reagents. The reagents used were Texas Red-dextran (70,000 molecular weight; Invitrogen); 1 μm , red fluorescent microspheres (Invitrogen); lipopolysaccharide (LPS) (from *Escherichia coli* O55:B5; Sigma-Aldrich); and MIP-2 (R&D Systems).

Thoracic suction window. We adapted a custom, thoracic suction window based on previously published designs⁹, by miniaturizing to a 4 mm internal diameter, and we fitted this with a 12 mm glass coverslip.

Surgical preparation. Mice were anesthetized with Ketamine (80 mg kg⁻¹) and Xylazine (12 mg kg⁻¹) i.p. and placed on a custom, heated microscope stage. PE-90 tubing was inserted into the trachea and sutured into place to facilitate mechanical ventilation with a rodent ventilator (Kent Scientific). Mice were ventilated with pressure control ventilation (inspiratory pressure = 12–15 centimeters of water (cmH₂O), a respiratory rate of 120 breaths per minute, a fraction of inspired oxygen of 0.5–1.0 and a positive-end expiratory pressure (PEEP) of 3 cmH₂O. Isoflurane was continuously delivered at 1% to maintain anesthesia and mice were given an i.p. bolus of PBS (1 ml) before the thoracic surgical procedure. The mice were then placed in the right lateral decubitus position and three left anterior ribs were resected and the left lung was carefully exposed. The thoracic suction window attached to a micromanipulator on the microscope stage was then placed into position and 20–25 mm Hg of suction was applied (Amvex Corporation) to gently immobilize the lung. The two-photon microscope objective was then lowered into place over the thoracic suction window and a 12 mm coverslip. For intravenous injections, the right jugular vein was cannulated with a 30 gauge needle attached to PE-10 tubing for injections of cells or intravascular dyes.

Two-photon microscopy. A custom resonant-scanning two-photon instrument⁷ contains a four-photomultiplier tube detector (R5929 Hamamatsu), collects data at video rate, and uses an Olympus XLUMP FL20XW (numerical aperture (NA) 0.95) objective with an overfilled back aperture with a fill-factor of approximately 1. Samples were excited with a 5-W MaiTai TiSapphire laser (Spectra-Physics) tuned to a wavelength of 910 nm, attenuated via a variable neutral density wheel to ~25–40% of power (0.175–0.28 W) and using emission wavelengths of 440/40 nm (for CFP), 505/20 nm (for EGFP), and 605/70 nm (for beads or dextran) were collected. A custom, four-dimensional acquisition module in VideoSavant

digital video recording software (IO Industries) or in Micromanager was used for image acquisition. For time-lapse acquisition, each *x-y* stack spans 240 μm \times 288 μm at an *x-y* resolution of 0.6 μm per pixel. For *z*-stacks, we collected data at a *z*-dimension resolution of 2 μm . *z*-dimension distances and averaged frames are indicated for each individual experiment.

Blood flow velocity experiments. Red, fluorescent microspheres (1 μm ; Invitrogen) were injected into the right, jugular vein and imaged using a fast acquisition mode at 30 fps. To measure cellular velocities, individual fluorescent protein-labeled mice were used. Imaris spot detection was used to locate the centroid of cells or beads, and the tracking function was used to determine instantaneous velocities (between time points) or average track speeds (average of instantaneous velocities for the entire observation period). All additional analyses were performed using Metamorph (Universal Imaging), Imaris (Bitplane Inc.) and Photoshop (Adobe Inc.) software.

Lung stretch injury. Lung stretch injury (ventilator-induced lung injury) was initiated by increasing the pressure controlled ventilation to 30 cmH₂O and decreasing the PEEP to 0 cmH₂O. Mice were also injected with Texas Red dextran (70,000 MW) via the jugular vein for the imaging of lung vascular leak.

MIP-2 and LPS-induced lung injury. Mice were intratracheally challenged with MIP-2 (5 μg ; R&D Systems) or LPS from *Escherichia coli* O55:B5 (Sigma-Aldrich) at 5 mg kg⁻¹.

Quantifying lung vascular permeability Alveolar spaces were defined by the absence of Actin CFP. Isosurfaces were drawn in the alveolar space using Imaris (Bitplane, Inc) manual surface creation tool. The relative amount of dextran within the space was determined by calculating the average red (Texas Red-dextran) intensity in the airspace.

Quantifying lung edema. The gravimetric method was used to measure the lung wet-to-dry weight ratio (grams/grams) as previously described^{19,27}. The right and left lungs were separately removed, weighed, placed in a drying oven at 55 °C for 48 h, and then weighed again to calculate the wet-to-dry weight ratio.

T-cell experiments. Activated ubiquitin-EGFP T cells were generated by incubating splenocytes and lymph node cells from an ovalbumin-specific T-cell receptor transgenic (OTII) \times Ub-EGFP mouse with ova peptide SIINFEKL (Sigma-Aldrich) and supplemented with recombinant mouse IL-2 (BD-Biosciences). They were transferred after 4 or 5 d of culture. Naïve CD2-RFP OTII cells were isolated and used immediately. A single cell suspension was isolated from lymph nodes and spleens of CD2 RFP/OTII TCR transgenic mice. Naïve CD4 T cells were purified using the Stemsep CD4 negative selection kit. T cells were transferred into actin-CFP mice via the jugular vein.

Statistics. Data is presented as mean \pm s.e.m. *P* values were determined by performing a two-tailed *t*-test. To determine the stability of the imaging setup, Pearson's correlation coefficient of actin-CFP fluorescence intensity was measured for every frame with respect to the first frame, using the 'co-localization' function in Imaris.

25. Sasmono, R.T. *et al.* A macrophage colony-stimulating factor receptor-green fluorescent protein transgene is expressed throughout the mononuclear phagocyte system of the mouse. *Blood* **101**, 1155–1163 (2003).
26. Hadjantonakis, A.K., Macmaster, S. & Nagy, A. Embryonic stem cells and mice expressing different GFP variants for multiple non-invasive reporter usage within a single animal. *BMC Biotechnol.* **2**, 11 (2002).
27. Faust, N., Varas, F., Kelly, L.M, Heck, S. & Graf, T. Insertion of enhanced green fluorescent protein into the lysozyme gene creates mice with green fluorescent granulocytes and macrophages. *Blood* **96**, 719–726 (2000).
28. Fukuda, N., Folkesson, H.G. & Matthay, M.A. Relationship of interstitial fluid volume to alveolar fluid clearance in mice: ventilated vs. in situ studies. *J. Appl. Physiol.* **89**, 672–679 (2000).